# Delayed Ignition of Autocatalytic Combustion Precursors: Low-Temperature Nanomaterial Binder Approach to Electronically Functional Oxide Films

**6 AUTHORS**, INCLUDING:

Myung-Gil Kim
Chung-Ang University
**29** PUBLICATIONS   **749** CITATIONS

SEE PROFILE

Jonathan Hennek
Nano Terra
**21** PUBLICATIONS   **696** CITATIONS

SEE PROFILE

Hyun Sung Kim
Pukyong National University
**884** PUBLICATIONS   **15,575** CITATIONS

SEE PROFILE

Antonio Facchetti
Northwestern University
**383** PUBLICATIONS   **22,236** CITATIONS

SEE PROFILE

# Delayed Ignition of Autocatalytic Combustion Precursors: Low-Temperature Nanomaterial Binder Approach to Electronically Functional Oxide Films

Myung-Gil Kim, Jonathan W. Hennek, Hyun Sung Kim,[§] Mercouri G. Kanatzidis,* Antonio Facchetti,* and Tobin J. Marks*

Department of Chemistry and the Materials Research Center, Northwestern University, 2145 Sheridan Road, Evanston, Illinois, 60208

**ⓢ** *Supporting Information*

**ABSTRACT:** Delayed ignition of combustion synthesis precursors can significantly lower metal oxide film formation temperatures. From bulk $In_2O_3$ precursor analysis, it is shown here that ignition temperatures can be lowered by as much as 150 °C. Thus, heat generation from ~60 nm thick $In_2O_3$ films is sufficient to form crystalline $In_2O_3$ films at 150 °C. Furthermore, we show that the low processing temperatures of sufficiently thick combustion precursor films can be applied to the synthesis of metal oxide nanocomposite films from nanomaterials overcoated/impregnated with the appropriate combustion precursor. The resulting, electrically well-connected nanocomposites exhibit significant enhancements in charge-transport properties vs conventionally processed oxide films while maintaining desirable intrinsic electronic properties. For example, while ZnO nanorod-based thin-film transistors exhibit an electron mobility of $10^{-3}$–$10^{-2}$ $cm^2$ $V^{-1}$ $s^{-1}$, encasing these nanorods within a ZnO combustion precursor-derived matrix enhances the electron mobility to 0.2 $cm^2$ $V^{-1}$ $s^{-1}$. Using commercially available ITO nanoparticles, the intrinsically high carrier concentration is preserved during nanocomposite film synthesis, and an ITO nanocomposite film processed at 150 °C exhibits a conductivity of ~10 S $cm^{-1}$ without post-reductive processing.
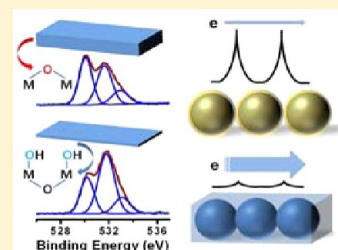
## INTRODUCTION

The future of low-cost macroelectronics depends critically on developing new solution-processable organic and inorganic materials,[1] understanding fundamental details of their charge transport[2] and thin-film microstructure evolution,[3] and perfecting unconventional fabrication methodologies.[4] In this field, metal oxides have been intensively investigated for application in various electronic components, spanning properties from those of insulators to semiconductors, to conductors.[5] Thus, depending on the metal type and composition, these materials may fulfill the required materials performance metrics such as the electrical conductivity required for an electrode, the large field-effect carrier mobility required for a semiconductor in a transistor, and the excellent insulating properties required for a wide variety of dielectrics, as well as thermal/electrical stability, environmental robustness, and optical transparency.[6] Moreover, cost-effective solution processing has been demonstrated for a variety of metal oxide semiconductors (e.g., ZnO, $In_2O_3$, a-IGZO, a-IGO, a-ITO, a-ZITO, a-ZTO; a = amorphous phase), conductors (e.g., ITO, FTO, ATO, AZO), and insulators (e.g., a-$ZrO_2$, a-$HfO_2$, a-$Al_2O_3$, a-$HfOSO_4$), using sol–gel, nanomaterial, chemical bath deposition (CBD), successive ionic layer adsorption and reaction (SILAR), and more recently, combustion precursor synthetic approaches, to cite just a few.[7]

Metal oxides and related nanomaterials have been used for diverse electronic applications, benefiting from their improved processability and intrinsic electronic structures, and are finding use in field-effect transistors, solar cells, IR detectors, and light-emitting devices.[7h,8] Devices designed from the bottom up have also been demonstrated using finely tuned metal or metal chalcogenide nanoparticles. Nevertheless, achieving effective interparticle carrier transport remains a challenge if any of these nanomaterials are to be implemented in electrical, magnetic, and/or optoelectronic applications.[8d] In most cases, proper electrical connectivity between the nanoparticles and subsequent carrier transport, are significantly hindered by the surface capping ligands used to solubilize the nanomaterial for processing. To increase carrier mobility in bulk nanoparticle arrays, various approaches have been explored to address this limitation, such as thermal annealing, post-ligand exchange, novel Zintl anion-based inorganic ligands, etc.[9] Importantly, most approaches aimed at enhancing interparticle electrical connectivity cannot be straightforwardly applied to emerging transparent and/or flexible electronics, especially oxide electronics. Typically, thermal treatment is applied to achieve pristine nanomaterial surface ligand removal and grain growth, as shown in Figure 1A. Although proper choice of the surface capping ligand can depress typical high-temperature processing requirements to as low as at 150 °C or less for some types of nanoparticles, the high melting points of metal oxides still
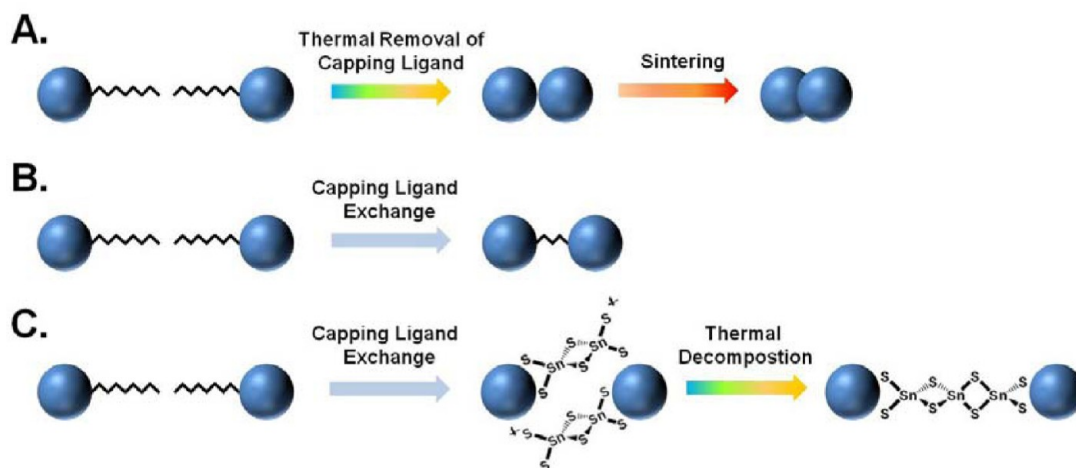
**Figure 1.** Approaches to enhancing interparticle electrical connectivity. (A) Surface ligand removal and sintering by high-temperature annealing. (B) Capping ligand exchange with short-length ligands. (C) Capping ligand exchange with thermally labile molecular Zintl anions.

require significantly higher processing temperatures to promote proper grain growth and/or particle interconnection and renders this approach incompatible with flexible plastic and even typical glass substrates.[9c,10] For example, ZnO nanoparticle-based thin-film transistors with field effect mobilities of $\sim 10^{-3}$ cm$^2$ V$^{-1}$ s$^{-1}$ have been demonstrated, but only after annealing at temperatures of $\sim 400$ °C.[10c,e] Some mobility enhancement over these metrics is achieved using aligned ZnO nanorods, thereby achieving mobilities of $\sim 0.1$ cm$^2$ V$^{-1}$ s$^{-1}$.[7h] For conducting ITO nanoparticles, typical annealing temperatures of >500 °C are required to achieve reasonable thin-film conductivities (>10 S cm$^{-1}$).[10d,11,12] As summarized in Figure 1B, surface ligand exchange with smaller ligands can improve carrier transport; however, the resulting mean interparticle distances still remain too large for high-mobility, bandlike transport.[8a,10b,13] Cross-linked short-chain ligands can only achieve conductivities of $\sim 10^{-1}$ S cm$^{-1}$ with 5 nm gold nanoparticles.[14] Figure 1C illustrates the dramatic change in surface ligand role from passive solution stabilizer to active charge transporter using thermally labile inorganic Zintl anions as nanoparticle ligands.[9b] Thus, capping 5 nm Au nanoparticles with the anionic Sn$_2$S$_6^{4-}$ ligand yields composites with conductivities as high as $\sim 200$ S cm$^{-1}$ after thermal conversion of the Sn$_2$S$_6^{4-}$ units into SnS$_2$ by 200 °C annealing.[9b] Furthermore, a field-effect mobility of 16 cm$^2$ V$^{-1}$ s$^{-1}$ was demonstrated with similarly processed In$_2$Se$_4^{2-}$-capped CdSe nanocrystal TFTs.[15] However, the small band gaps of the chalcogenide mataerials prepared from the Zintl anions degrades the optical transparency, and the materials are likely oxidation-unstable under ambient.[16]

Recently, our laboratory reported combustion synthesis, using soluble metal oxide precursors, as a new generalizable approach to low-temperature, solution-processed metal oxide thin-film electronics.[17] To overcome the endothermic nature of typical hydroxide/alkoxide conversions into metal oxides, the high internal energy of combustion precursors is used to minimize the external energy input required for film growth. The self-catalytic, highly exothermic nature of the precursor transformation affords the corresponding oxide product films at sufficiently low temperatures to be compatible with flexible plastic substrates. For example, we showed that In$_2$O$_3$ and ITO combustion precursors can be used to fabricate solution-processed oxide thin-film electronics. Thus, excellent thin-film

transistor (TFT) device performance with $\mu_e^{\text{FET}} \approx 10$ cm$^2$ V$^{-1}$ s$^{-1}$ for In$_2$O$_3$-based TFTs and good electrical conductivities of $\sim 10$ S cm$^{-1}$ for ITO, were demonstrated at processing temperatures as low as 200 °C for In$_2$O$_3$ and 225 °C for ITO.[17] These successful demonstrations confirm that combustion approaches are a promising next-generation solution-processing method for thin-film electronics. These results, combined with the aforementioned limitations of conventional nanomaterial-based devices, now raise the interesting question of whether combustion synthesis can be used to enhance the electronic connectivity between preformed metal oxide nanostructures, of what materials can be produced, and how their performance compares with previous approaches. The goal is to achieve closely connected oxide nanoparticles at low temperatures so that the intrinsic electronic character of the nanomaterial is preserved but with enhanced interparticle electrical communication.

Figure 2 shows a schematic of the evolution of film charge carrier transport performance as a function of increased oxide nanomaterial connectivity. For conventional approaches as
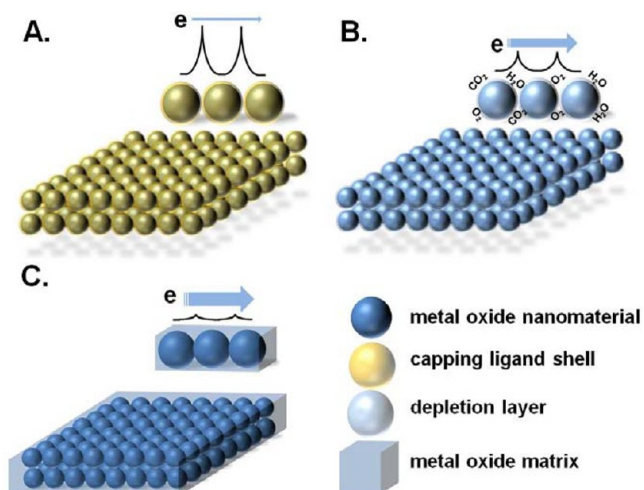


**Figure 2.** Carrier transport dependence on metal oxide nanomaterial connectivity. (A) Surface ligand capped nanomaterial array. (B) Depleted bare nanomaterial array. (C) Nanomaterial and corresponding matrix combined array.
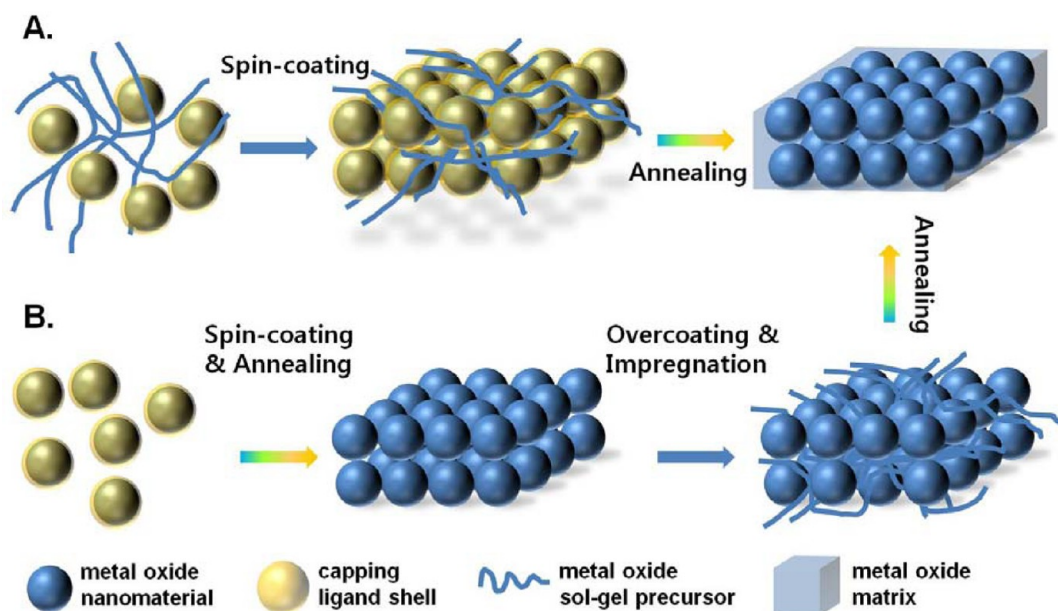
**Figure 3.** Fabrication of structurally/electrically well-connected nanomaterial arrays. (A) One-step deposition using a sol−gel/nanomaterial mixture. (B) Two-step fabrication using an overcoating and impregnation approach.

shown in Figure 2A, bulky surfactant ligands result in poor interparticle connectivity and poor charge transport through the film.[18] Moreover, schemes for ligand removal are generally ineffective in preserving particle carrier mobility for transparent metal oxide nanomaterial ensembles. Following deligation, the exposed interfaces between particles still inhibit carrier transport across the large-grain boundary potentials arising from absorbed $O_2$ or $CO_2$ depletion layers, as in Figure 2B.[19] However, once the particles are properly connected by sintering or surrounded by a compatible matrix, ideally having the same nanomaterial composition or at least having an energetically aligned band edge (Figure 2C), charge transport should be facile with small-grain boundary potential barriers. The well-connected nanomaterial array can be deposited by using either a codissolved nanomaterial/matrix precursor mixture or a separate nanomaterial combined with an overcoating matrix precursor. These scenarios are illustrated in Figure 3.

In this contribution we demonstrate two important new concepts. First, we report further mechanistic details regarding the thin oxide film combustion synthesis process we reported earlier, including the observation of ignition phenomena at even lower temperatures than in the previous work. Second, by combining the predefined character of appropriate nanomaterials with our low-temperature combustion precursor technique, we achieve conducting ITO at temperatures as low as 150 °C with a conductivity of ∼10 S cm$^{-1}$, and ZnO field-effect transistor at temperatures as low as 225 °C with $\mu_e^{FET} \approx$ 0.2 cm$^2$ V$^{-1}$ s$^{-1}$.

## ■ EXPERIMENTAL SECTION

**Combustion Precursor Preparation.** The In and Zn precursor solutions were prepared by dissolving 386.1 mg $In(NO_3)_3 \cdot 4.46H_2O$ in 2.5 mL 2-MeOEtOH or 297.6 mg $Zn(NO_3)_2 \cdot 6H_2O$ in 5.0 mL 2-MeOEtOH and then adding 0.2 mL acetylacetone. After complete dissolution of the metal salts, 114 μL 14.5 M $NH_{3(aq)}$ is added and the solution aged for 12 h. For the Sn precursor, 189.6 mg $SnCl_2$ and 80.1 mg $NH_4NO_3$ are dissolved in 2.5 mL 2-MeOEtOH, and then 0.2 mL acetylacetone is added. After dissolution of all salts, 57 μL 14.5 M

$NH_{3(aq)}$ is added and the solution aged for 12 h. For the ITO precursor solution, the In and Sn solutions are mixed to achieve an In/Sn = 9:1 mol/mol ratio, and were then stirred for 1 h in a closed vial before use. The mother solutions with fixed chemical ratios are diluted with 2-MeOEtOH for growing thinner films.

**Nanomaterial Precursor Preparation.** The ITO nanoparticle sol (30 wt % in isopropyl alcohol, <100 nm particle size, product #700460) was purchased from Sigma-Aldrich. The ITO nanosol was diluted to 20 wt % in isopropyl alcohol. The 60−80 nm ZnO nanorods were synthesized following the reported methods of Sun et al.[7h]

**Precursor Characterization.** Thermal analyses were carried out on about 10 mg samples prepared from 70 °C vacuum-dried combustion precursor solutions or 25 °C air-dried nanomaterial dispersions. The thermogravimetric analysis (TGA) and differential thermal analysis (DTA) measurements were performed on a Shimadzu TGA-50 thermogravimetric analyzer and a Shimadzu DTA-50 thermal analyzer, respectively. The thermogravimetric analysis−mass spectrometry (TGA-MS) measurements were carried out on a Mettler STARe ThermoGravimetric Analyzer, TGA/sDTA851e, coupled to a Balzers ThermoStar Mass Spectrometer. The heating rate was 10 °C min$^{-1}$ up to the target temperature under a 20 mL min$^{-1}$ Ar flow for TGA-MS and a 20 mL min$^{-1}$ air flow for TGA and DTA, using aluminum pan sample containers. A INEL CPS120 X-ray powder diffractometer with graphite monochromatized Kα radiation was used for X-ray powder diffraction measurements.

**Film Deposition and Thin Film Transistor Device Fabrication.** The 20 wt % ITO nanosol in isopropyl alcohol was spin-coated at 5000 rpm for 30 s onto 300 nm $SiO_2$/p+Si substrates, and the samples were then annealed at the desired temperature (100−400 °C) for 30 min under air. The ∼30 mg/mL ZnO nanorod (∼ 60−80 nm × 10 nm) suspension in chloroform/methanol (3:1) was spin-coated at 2000 rpm for 30 s on top of HMDS-treated 300 nm $SiO_2$/p+Si wafers, and the samples were then annealed at the 225 °C for 30 min under air. Overcoating of the combustion precursor was achieved by spin-coating the ITO or ZnO precursor at 2000 rpm for 30 s, and subsequently annealing at the desired temperature (200−500 °C) for 30 min under air. The overcoating was repeated as needed to fill any voids. The post-reduction treatment of the ITO samples was carried out under an $H_2$ atmosphere for 2 h at the same temperatures as for the $T_{anneal}$ < 300 °C samples, or at 300 °C for the $T_{anneal} \geq$ 300 °C samples. For ZnO nanorod TFTs, Al source and drain electrodes of 100 nm thickness were deposited by thermal evaporation (pressure ∼10$^{-6}$ Torr) through a shadow mask, affording channel dimensions of

100 $\mu m$ ($L$) × 5000 $\mu m$ ($W$) with appropriate precautions for TFT measurement accuracy.[20]

**Thin Film Microstructural Characterization.** Grazing incident angle X-ray diffraction (GIAXRD) scans were measured with a Rigaku ATX-G thin-film diffraction workstation using Cu K$\alpha$ radiation coupled to a multilayer mirror. XPS spectra were recorded on an Omicron ESCA Probe system with a base pressure of $8 \times 10^{-10}$ mbar (UHV), using a monochromated Al K$\alpha$ X-ray source at $h\nu = 1486$ eV. Film surface morphologies were imaged with AFM and SEM using a Veeco Dimension ICON PT AFM System and a Hitachi S-4800-II FE-SEM. The ITO film thickness was determined by cross-sectional SEM images and/or with a J.A. Woollam M2000U spectroscopic ellipsometer.

**Thin Film Electrical Characterization.** The conductivity of ITO films was measured with a Keithley 2400 source meter using the four-probe method. Hall measurements on ITO films were carried out with an Ecopia HMS-3000 Hall measurement system using the Van der Pauw method. The ZnO TFT device characterization was performed on a customized probe station in dry air with a Keithley 6430 subfemtometer and a Keithley 2400 source meter, operated by a locally written Labview program and GPIB communication.

TFT performance parameters, saturation mobility ($\mu_{Sat}$), and current on/off ($I_{on}/I_{off}$) ratio were evaluated from transfer plots with the conventional metal-oxide-semiconductor field effect transistor (MOSFET) model described in eq 1: where $C_i$ is the capacitance per unit area of the dielectric layer, $L$ and $W$ are the channel length and width, respectively.[21]

$$\mu_{Sat} = \left( \frac{\partial \sqrt{I_{DS}}}{\partial V_G} \right)^2 \frac{2L}{WC_i}$$

(1)

## RESULTS AND DISCUSSION

To demonstrate a new concept in enhancing metal oxide nanomaterial connectivity via combustion processing,[17] we first investigate details of the combustion chemistry for $In_2O_3$, ITO, and ZnO precursors for bulk as well as thin film samples of different thicknesses and, for a given mass/thickness and temperature, for different processing times. In particular, we analyze the time scales over which these processes occur for the different metal oxides, since this can provide further information on reducing annealing temperatures. Next, we apply the concept of a self-heat-generating chemical precursor, i.e., a combustion precursor,[17] to enable interparticle electronic connectivity at low temperatures for ITO nanoparticles and ZnO nanorods.

**Delayed Combustion Precursor Ignition.** To determine how the overall mass dependence of the reactants affects the combustion process, we performed bulk sample and thin-film experiments to identify the lowest possible temperatures which enable combustion synthesis. It is known that combustion precursors usually require some degree of predecomposition before autocatalytic vigorous combustion is initiated. Thus, a small amount of reactants cannot generate the critical amounts of predecomposed species necessary for ignition.[22] For thin films, the loss of autocatalytic species due to high surface-to-volume ratios can suppress rapid combustion and result in poor conversion of precursor into product.

From the thermal analysis of 70 °C vacuum-dried $In_2O_3$, ITO, and ZnO combustion precursors, we observe 150 °C to be the minimum temperature for the conversion of various acetylacetone-nitrate-based systems, as shown in Figures 4A–C. By lowering the maximum temperature from the immediate ignition temperature of ~200 to 150 °C, there is a significant delay in the abrupt exotherm ("ignition"). In the case of ~10 mg $In_2O_3$, ignition occurs in ~5 and 35 min after holding the
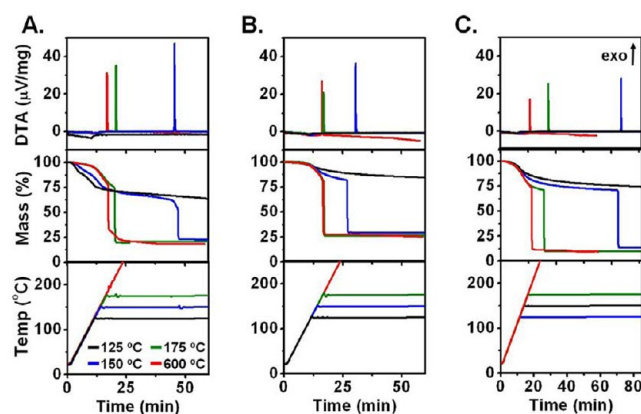


**Figure 4.** Bulk thermal analyses (DTA and TGA) of metal oxide combustion precursors with extended annealing times at the color-coded temperatures. (A) $In_2O_3$ precursor. (B) ITO (In/Sn = 9:1 mol/mol ratio) precursor. (C) ZnO precursor. The temperatures shown in the bottom-left panel indicate the maximum/equilibrium temperature of the temperature–time ramp profile.

temperature at 175 and 150 °C, respectively. If the maximum isothermal temperature is lowered to 125 °C, $In_2O_3$ precursor ignition does not occur within 1.0 h using the same assessment methodology. From the thermal analysis data, it can be seen that the same behavior is observed for ITO and ZnO, except that the ignition time differs. Once ignition occurs, the powder X-ray diffraction (PXRD) spectra of the ignition products correspond well to the corresponding $In_2O_3$, ITO, and ZnO data from the PXRD database (Figures 5A–C). The $In_2O_3$
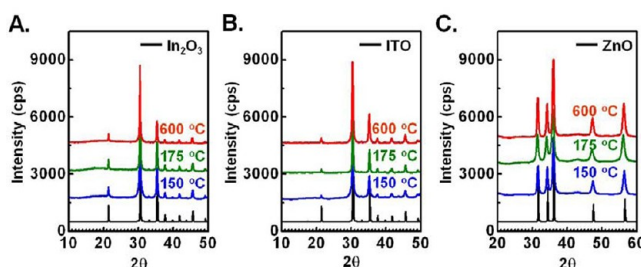


**Figure 5.** $\theta$–$2\theta$ PXRD spectra of the metal oxide combustion precursor decomposition products with each scan corresponding to the indicated heating profile in the thermal analyses of Figure 4. (A) $In_2O_3$ precursor. (B) ITO (In/Sn = 9:1 mol/mol ratio) precursor. (C) ZnO precursor.

combustion precursor thermolysis was also investigated by TGA-MS for both the continuous and the 150 °C isothermal heating profiles. Indium oxide was chosen as a model system due to the simplicity of the final decomposition products ($In_2O_3$, $CO_2$, $H_2O$, and $N_2$ as ideal combustion products) and its importance in electronic applications as the mother compound for transparent conducting oxides (TCO) and transparent oxide semiconductors (TOS).[23] As shown in A and C of Figure 6 for continuously heated samples, the initial mass loss and thermolysis of the organic fuel are identified by $m/e$ peaks at 43 ($CH_3CO$), 44 ($CO_2$), and 58 ($CH_3COCH_3$). In addition to the organic fuel, the simultaneous generation of oxidizing species is identified at 16 (O) and 30 (NO). From the TGA-MS results (Figure S1 in Supporting Information and Figure 6C and D), the principal products of sol–gel precursor combustion can be described by eq 2.
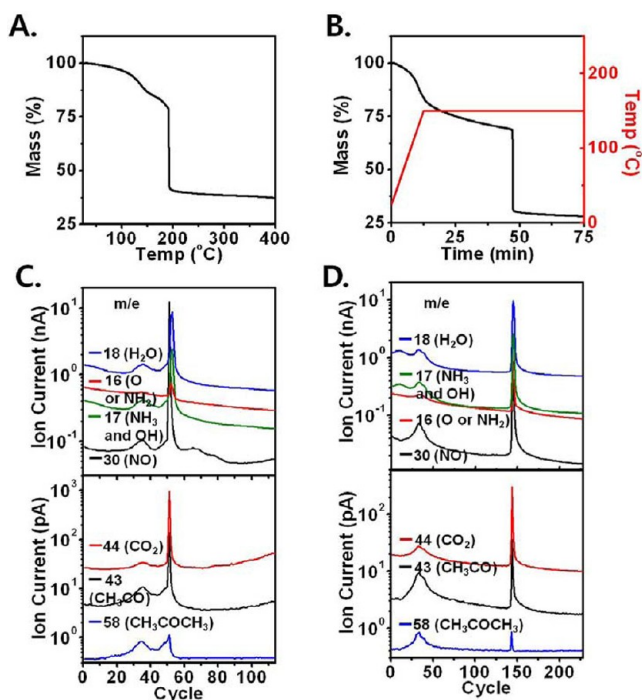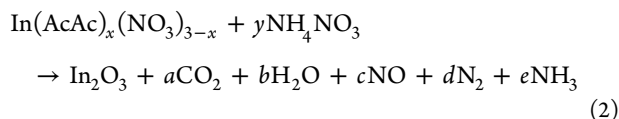
**Figure 6.** TGA-MS monitoring of $In_2O_3$ combustion precursor conversion under Ar. TGA with continuous heating up to 400 °C (A) and with isothermal heating at 150 °C (B), and the corresponding MS of gaseous products (C) and (D), respectively.

$$In(AcAc)_x(NO_3)_{3-x} + yNH_4NO_3$$

$$\rightarrow In_2O_3 + aCO_2 + bH_2O + cNO + dN_2 + eNH_3 \tag{2}$$

As previously reported for the simple thermal decomposition of metal acetylacetonates, initial loss of the acetylacetonate ligand and its decomposition initially release acetylacetone and acetone.[24] $CO_2$ evolution is observed at temperatures above those for ligand scission. Unlike simple thermal decomposition,

the presence of highly oxidizing species further accelerates the decomposition process to $CO_2$, even at temperatures as low as ~130 °C. From the reported results for the $Fe(NO_3)_3$ combustion process, it appears that precursor ignition occurs due to oxidizing species generated via $HNO_3$ formation and its conversion to a chain reaction initiator.[22] Although fuel oxidation can, in principle, occur at low temperatures, the autocatalytic (chain) reaction cannot be initiated if there are stoichiometrically insufficient quantities of oxidizer and fuel available. However, once the precursor reaches the ignition temperature, all organic fuel can be fully oxidized, with significant generation of $H_2O$, $CO_2$, $N_2$, $NH_3$, $NO$, and $O_2$. In the case of delayed ignition, as shown in B and D of Figure 6, the same thermal decomposition products are observed except that there is a distinct temporal separation of the initial slow decomposition and the abrupt mass loss. Thus, for the $In_2O_3$ precursor, the gradual mass loss occurs within ~47 min before abrupt mass loss. The delay time for ignition is likely the induction period in the chain reaction, and the buildup of such chain reaction carriers thus requires an induction period.[25]

**Sample Size Dependence of the Combustion Precursor.** Although all combustion-decomposed bulk samples clearly afford the corresponding crystalline metal oxide phases as judged from the PXRD data, a more interesting behavior is observed in the corresponding thin film chemistries. Here the large surface/volume ratio enables efficient mass and heat exchange compared to the bulk samples. Since the combustion reactions depend on internal heat accumulation and the volatile oxidizing initiator concentration, the degree of heat loss and outgassing is expected to depend on the film thickness. Furthermore, an important question arises as to whether these factors also affect the reaction kinetics, resulting in a different time evolution of the products. Because of its structural simplicity and high dehydration temperatures, $In_2O_3$ was again chosen as the model system to study the detailed thickness and kinetics dependence of the combustion conversion process for films.[26] Thus, solution-processed metal oxide films were fabricated by spin-coating while varying the precursor concentration and spin rate to control the final film thickness.
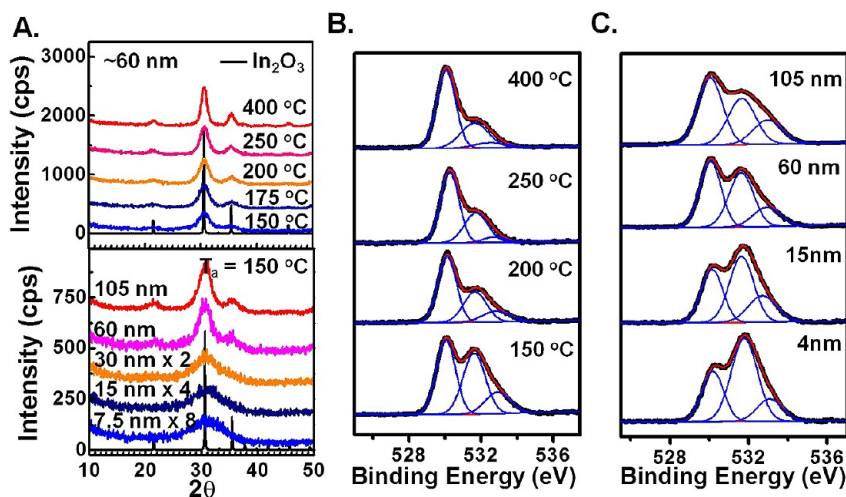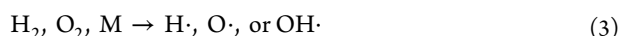


**Figure 7.** Thin film characterization of the combustion process to produce $In_2O_3$ films. (A) GIAXRD scans of 60 nm thick $In_2O_3$ films annealed at the indicated temperatures, and (below) 150 °C annealing of 60 nm thick films with initial thickness varied from 7.5 to 105 nm for each deposition. The reflections at the bottom in black are from the PXRD database. (B) XPS spectra of 60 nm $In_2O_3$ films annealed at the indicated temperatures. (C) XPS spectra of 150 °C annealed $In_2O_3$ films with thickness varied from 4 to 105 nm for each deposition. In (B) and (C), the dark-blue lines indicate experimental data, while the red and light-blue lines are fitted curves.

In the grazing incidence angle X-ray diffraction (GIAXRD) analysis shown in Figure 7A, the 150 °C annealed ~60 nm thick $In_2O_3$ film clearly shows crystalline $In_2O_3$ reflections. Note that the conversion and crystallization of $In_2O_3$ films occurs at 150 °C—far lower than the reported dehydration temperature of $In(OH)_3$ at ~270 °C and the crystallization temperature of amorphous $In_2O_3$ films at ~180 °C.[26,27] Without sufficient time for lattice relaxation or grain growth to yield highly crystalline films during the rapid combustion process, annealing the films from 150 to 400 °C enhances film crystallinity as shown in the temperature-dependent GIAXRD studies of 60 nm $In_2O_3$ film growth in Figure 7A. However, highly textured films are also formed at the lowest temperatures. The metal oxide lattice formation at low temperatures is also confirmed by the X-ray photoemission (XPS) spectra in Figure 7B. The 530.1, 531.8, and 532.8 eV features are assigned to metal−oxygen−metal (M−O−M) lattice, metal−OH, and adsorbed surface species ($CO_2$, $H_2O$, etc.), respectively.[28] The dominant M−O−M peak at 150 °C confirms formation of crystalline $In_2O_3$.

The critical sample size dependence of the indium oxide structural transformations is confirmed from a thickness dependence study of 150 °C annealed $In_2O_3$ films. In Figure 7A, the ~60 nm and ~105 nm thick films are crystalline $In_2O_3$; however, multiple thin-film depositions yielding the overall ~60 nm thickness consist of amorphous indium hydroxide. To confirm that the broad GIAXRD peaks from the thin-layer depositions are not due to smaller crystallite sizes, O1s XPS analysis was performed for films having varied thicknesses, as shown in Figure 7C. The ratio of the M−O−M lattice peak to that for M−OH is increased as the film thickness is incremented. Although 60 nm thick $In_2O_3$ films also afford crystalline $In_2O_3$, the thicker 105 nm films achieve far greater conversion into the metal−oxygen−metal lattice microstructure. Considering that the principal driving force for metal oxide lattice formation from the combustion precursor is internally generated heat, the increased surface/volume ratio for thinner films is the major source of significant heat loss and low internal reaction temperatures. Furthermore, the large thin-film surface/volume ratio is expected to facilitate loss of the volatile oxidizer (in situ generated $HNO_3$, $NO_2$, $O_2$) or fuel (acetylacetone, acetone, etc), yielding a less effective fuel/oxidizer ratio and/or insufficient amounts of fuel and oxidizer for ignition. For example, consider the relatively simple $O_2$ and $H_2$ combustion reactions in eqs 3−8:[29]
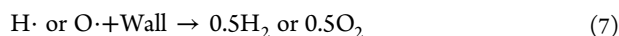
*Initiation:*

$$H_2, O_2, M \rightarrow H\cdot, O\cdot, \text{ or } OH\cdot \tag{3}$$

*Chain Branching:*

$$H\cdot + O_2 \rightarrow HO\cdot + O\cdot \tag{4}$$

$$O\cdot + H_2 \rightarrow OH\cdot + H\cdot \tag{5}$$

*Chain Propagation:*

$$H_2 + OH\cdot \rightarrow H_2O + H\cdot \tag{6}$$

*Termination:*

$$H\cdot \text{ or } O\cdot + Wall \rightarrow 0.5H_2 \text{ or } 0.5O_2 \tag{7}$$

$$H\cdot + O_2 + M \rightarrow HO_2 + M \tag{8}$$

Here M represents an inert third body. Although $HO_2\cdot$ is a radical, it is unreactive relative to OH· and H· radicals. It is typically treated as a stable compound in this mechanism. To maintain chain propagation and to further increase chain branching, the reaction requires a proper $O_2/H_2$ ratio and total concentrations. Thus, significant loss of the initiating oxidizer or fuel due to volatility can terminate branched chain reactions in the combustion process. Although thicker film combustion conversion is more efficient, the electrical performance of these films may suffer because of the porous morphology due to gaseous product outgassing.[17] Thus, the optimal film thickness is a compromise between efficient conversion and desired morphology.

From GIAXRD and XPS data (Figure S2 in Supporting Information [SI]), similar low decomposition temperatures are confirmed for combustion precursor-derived ZnO thin films. Unlike $In_2O_3$, ZnO has far lower dehydration and crystallization temperatures—less than 150 °C.[7g,30] Thus, if the organic ligands or stabilizers in a ZnO sol−gel precursor are removed at low temperatures, the low dehydration and crystallization temperatures enable efficient metal oxide lattice formation and observable crystallization at very low annealing temperatures ($T_{anneal}$ < 150 °C). For example, a $Zn(O_2CCH_3)_2$-based sol−gel precursor requires high annealing temperatures, over 300 °C, to remove the organic ligands.[31] In marked contrast, for a ZnO combustion precursor, the organic ligand or stabilizer can be effectively removed via formation of a redox pair with the nitrate ion. With a combustion precursor, similar crystalline ZnO films are obtained near 160 °C, regardless of the annealing temperature. Although the self-generated combustion energy cannot contribute significantly to dehydration and crystallization for the low-temperature conversion of a metal hydroxide to the corresponding metal oxide, combustion precursors can clearly be regarded as promising candidates for low-temperature solution processing of metal oxide films.

**Nanomaterial Precursor and Nanocomposite Fabrication and Characterization.** The properties of nanocompsites can be tuned by changing several parameters, such as nanomaterial composition, size, shape, and the combustion precursor composition. For example, improved electron transport was reported with ZnO nanorods compared to ZnO nanoparticles.[32] Also, various combustion precursor systems can be used as linker materials.[33] To test the feasibility of combustion precursor systems as low-temperature binders of oxide nanomaterials, we fabricated and characterized TCO films and FETs based on tin-doped indium oxide (ITO) and ZnO (vide infra). These oxides were selected because, in contrast to $In_2O_3$, the corresponding nanomaterial syntheses for stable suspensions are well established.[8a,34] Thus, commercial sources are available for ITO and ZnO nanoparticles. Indeed ZnO nanomaterial-based FETs and ITO nanoparticle-based TCOs have been reported by several research groups.[10b,11,12,18,35]

Since stable nanoparticle suspensions require functionalization with proper surfactants,[8a,34a,36] efficient surface ligand removal is critical to achieve acceptable charge transport. Here surface ligand removal is assayed by TGA of dried nanomaterial suspensions. The phase purity of the pristine nanomaterials was first verified vs the PXRD database. The ITO nanoparticle dispersion in isopropyl alcohol was purchased from Sigma-Aldrich, and the TGA plot exhibits negligible mass loss up to 600 °C (Figure 8A below). The PXRDs of the dried ITO dispersion in Figure 8B confirm clean conversion to the $In_2O_3$
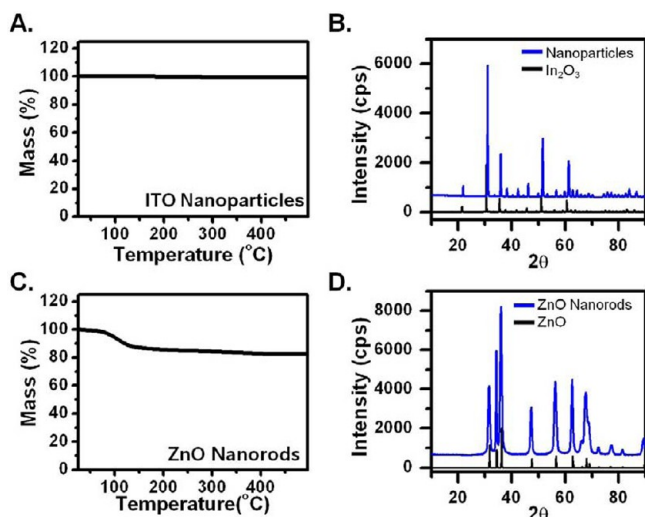
**Figure 8.** Bulk analysis of oxide nanomaterials. (A) TGA of a dry ITO nanoparticle dispersion (purchased from Aldrich). (B) $\theta$−$2\theta$ XRD of the dry ITO nanoparticle dispersion in Figure 7A. (C) TGA of a dry ZnO nanorod dispersion, synthesized as in ref 7h. (D) $\theta$−$2\theta$ XRD of a 100 °C annealed ZnO nanorod dispersion; below: ZnO. The reflections at the bottom in black are from the PXRD database.
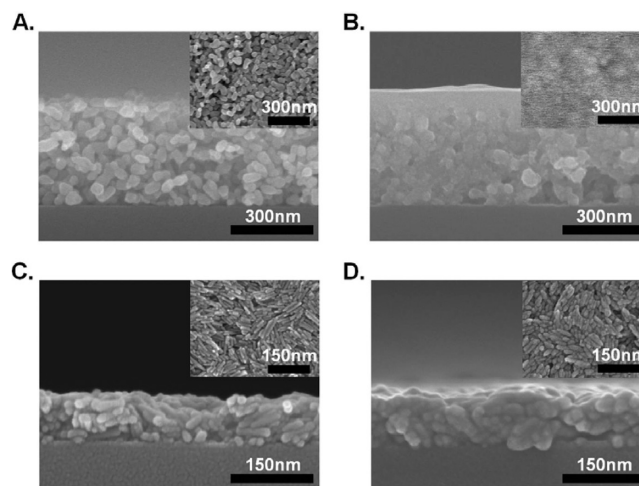


**Figure 9.** SEM images of nanomaterial and composite films. (A) and (B) Cross-section and plane view (inset) SEM images of as-deposited ITO nanoparticles (A) and coated with four overlayers of combustion-derived ITO nanocomposite film (B). (C) and (D) Cross-section and plane view (inset) SEM images of as-deposited ZnO nanorod film (C) and two-layer combustion ZnO-overlayer-coated ZnO nanorod film (D).

phase. The ZnO nanorod dispersion in MeOH/chloroform was synthesized according to a literature procedure,[7h] and TGA analysis of the dry ZnO dispersion (Figure 8C) indicates removal of *n*-octylamine from the ZnO nanorods below 150 °C, while the XRD of the 100 °C annealed dispersion in Figure 8D agrees well with the ZnO data in the database.

To achieve a flexible deposition methodology and better property control over the metal oxide nanocomposite film formation, the metal oxide nanomaterial deposition and connection processes were separated. Although a one-step deposition in which the nanomaterial is suspended in the precursor solution might at first appear to be a simpler film deposition process, preliminary experiments indicated that achieving stable solutions is problematic, and this will be a topic of a future study. However, here we report the successful integration of the nanomaterials with a combustion precursor binder by using an overlayer coating and impregnating it into the nanomaterial matrix. The morphologies of the spin-coated pristine nanoparticle films and subsequent composites coated/impregnated with combustion-derived overlayers were investigated by SEM and AFM (Figure 9 and Figures S3−S4 [SI]). In the cross-sectional SEM images, A and B of Figure 9, the ~380 nm thick ITO nanoparticle film microstructure is preserved as a ~440 nm thick ITO nanocomposite film after overcoating/impregnating. It can be seen that the overcoated combustion ITO primarily fills voids between the ITO nanoparticles, preserving optimal morphology even after multiple thermal treatments at 400 °C. This overlayer coating and void filling are also evident from the significant reduction of voids and particle features in the plane view SEM images in the insets of A and B or Figure 9. Furthermore, the RMS surface roughness changes from 15 nm (without an overlayer) to 5 nm (with 4 overlayers) measured from the AFM images in Figure S4 (SI), verifying the void and roughness reduction. The low annealing temperatures ($T_{anneal}$: 150−400 °C) used in our study enable smooth film deposition without significant crystallization, noting that grain coalescence processes can increase film roughness.[10d] For the case of the initially well-

packed ZnO nanorods shown in Figure 9C and combustion-overcoated/impregnated nanorods in Figure 9D, the formation of more interconnected ZnO domains is evident. Thus, it is possible to achieve significantly greater oxide nanoparticle film structural interconnectivity using this combustion coating/impregnation approach.

**Transport Properties of Nanomaterials and Composite Films.** The present structurally well-connected nanocomposite morphologies can significantly enhance carrier transport in metal oxide nanocomposite films. For the demonstration of actual applications, ZnO nanorod-based TFTs and ITO nanoparticle-based TCO films were fabricated. Carrier transport enhancement was first confirmed with the ZnO nanorod-based TFTs. In Figure 10, the field effect
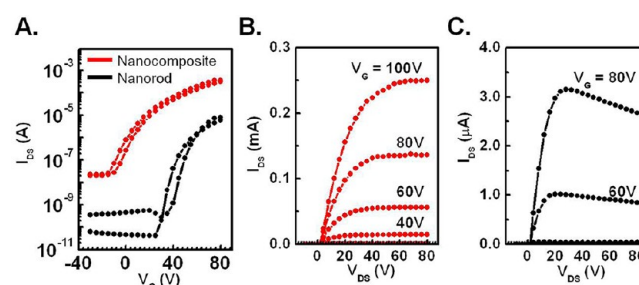


**Figure 10.** Representative transfer and output plots for ZnO-based TFTs having the structure, Si/SiO$_2$ (300 nm)/ZnO/Al (100 nm), $L$ = 100 $\mu$m, $W$ = 5000 $\mu$m. (A) Transfer plots for ZnO nanorod-based (black line) and nanocomposite-based (red line) TFTs. (B) Output plot for a ZnO nanocomposite-based device. (C) Output plot for ZnO nanorod device.

mobility is enhanced 20−200×, from $10^{-3}$−$10^{-2}$ cm$^2$ V$^{-1}$ s$^{-1}$ to 0.2 cm$^2$ V$^{-1}$ s$^{-1}$ with $I_{on}/I_{off} \approx 10^3$ using the present nanorod combustion overcoating/impregnation technique at 225 °C. The combustion precursor-derived ZnO films alone show poor morphology and yield inactive TFT devices (Figure S5 [SI]). In contrast to these observations, conventional ZnO sol−gel

binder-connected ZnO nanorod TFTs exhibit only a 5-fold increase in field effect mobility with 270 °C annealing.[7h] Some improvement over this performance is achieved in recently reported low-temperature solution-processed ZnO TFTs having aligned and random ZnO nanorods with post-growth hydrothermal treatment: ~1.2−1.4 (aligned) and ~0.4−0.6 (random) $cm^2 V^{-1} s^{-1}$ at 230 °C on $Si/SiO_2$; aqueous $Zn(OH)_x(NH_3)_y^{(2−x)+}$ precursor: ~0.7 $cm^2 V^{-1} s^{-1}$ at 200 °C on $Si/SiO_2$.[7g,h,32] The present proof-of-concept results showing charge transport enhancement in combustion precursor interconnected nanomaterials is clearly a different approach.

The predefined high free carrier concentrations of ITO nanoparticles can be utilized for low-temperature processed TCO films.[11a,34a,37] For combustion-processed ITO films, although crystalline ITO is obtained at 200 °C, the minimum processing temperature required for significant conductivities is ~250 °C, followed by post-annealing treatment with $H_2$.[17] From Figure 11A it can be seen that a reasonable conductivity
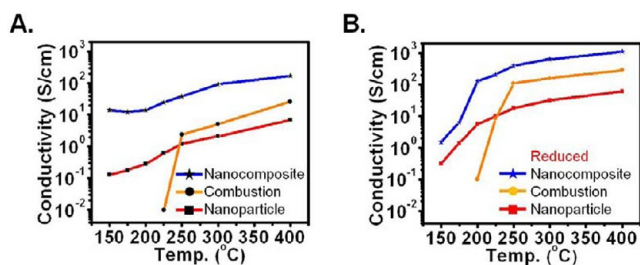


**Figure 11.** Conductivity of nanocomposite, combustion-processed, and nanoparticle-based ITO films with and without $H_2$ treatment, as function of processing temperature. (A) Conductivity of as-deposited films measured under air. (B) Conductivity of a film after 2 h reductive $H_2$ treatment.

of ~10 S $cm^{-1}$ is obtained for the nanocomposite after processing at 150 °C without further reduction. On annealing at higher temperatures, the conductivity increases to ~170 S $cm^{-1}$ for 400 °C processing of the ITO nanocomposite films. Generally high-temperature annealing of ITO films increases conductivity via dopant activation and/or oxygen vacancy generation.[38] Also, high-temperature annealing of nanoparticle-based ITO films significantly improves electron mobility through reduction of structural distortion, grain size growth, and improved crystallinity.[11a,35] From the Hall effect measurements in Figures 12A and 13A, it can be seen that increases in electron mobility are the primary origin of the conductivity
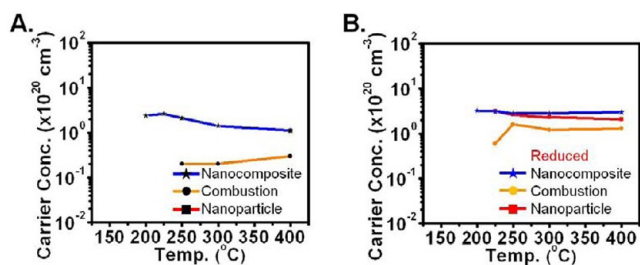


**Figure 12.** Carrier concentrations of nanocomposite, combustion, nanoparticle-based ITO films with and without $H_2$ treatment as function of processing temperature. (A) Carrier concentration of as-deposited ITO films under air. (B) Carrier concentration of ITO films after 2 h $H_2$ reductive processing.
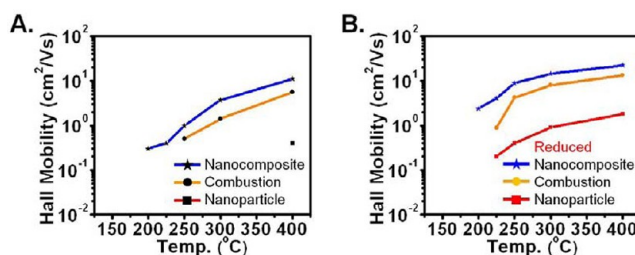


**Figure 13.** Hall mobility of nanocomposite-, combustion-, and nanoparticle-derived ITO films with and without reductive $H_2$ treatment, as function of processing temperature. (A) Hall effect mobility of as-deposited ITO films under ambient air. (B) Hall effect mobility of ITO films after 2 h $H_2$ reductive processing.

enhancement, and that the carrier concentration in the high-temperature annealed nanocomposite falls with ITO nanoparticle oxidation under ambient air. For the combustion precursor- and nanoparticle-derived films, an order of magnitude lower value is typically obtained. Although some low-temperature annealed, low-mobility samples did not give definitive Hall effect values, the comparison between measured samples reveals the origin of the conductivity enhancement in the present composites. From the Hall effect measurements in Figures 12A and 13A, the superior performance of the composite derives from the synergetic combination of predefined intrinsic properties and carrier transport enhancement. The low mobility of the nanoparticle films and low carrier concentrations of the simple combustion precursor films are the reason for the low conductivities. Note that the 1 S $cm^{-1}$ value, a reasonable metric for low performance applications, can be obtained with 250 °C annealing for combustion precursor- and nanoparticle-derived ITO films. To achieve conductivities approaching those of the 150 °C annealed nanocomposite films (~10 S $cm^{-1}$), requires 400 °C annealing of the combustion precursor- and nanoparticle-derived films.

To further increase ITO nanocomposite conductivity, post-reductive treatment under $H_2$ was carried out which is known to be effective in generating oxygen vacancies in metal oxide semiconductors.[39] From Figure 12B, it can be seen that $H_2$ reductive processing significantly enhances the conductivity of the present ITO films. In addition to the previously reported combustion precursor-derived films, the conductivity of the present nanoparticle films is also increased due to reduction of the oxidized ITO nanoparticles. Note also that oxidized grain boundaries are known to create a large potential barrier and have lower carrier mobilities.[19a] Unfortunately, reduction at 300 °C is insufficient to completely recover the as-prepared ITO nanoparticle carrier concentrations, judging from the higher carrier concentrations in the 225 °C reduced films shown in A and B or Figure 12. Thus, low processing temperatures are important to preserve the predefined intrinsic ITO nanomaterial transport properties. For the nanocomposite-derived films, a significant reduction in processing temperature, from 300 to 200 °C, is possible while maintaining conductivities >100 S $cm^{-1}$ with carrier concentrations ~3 × $10^{20}$ $cm^{-3}$ and electron mobilities ~2.4 $cm^2 V^{-1} s^{-1}$, as shown in Figures 11B, 12B, and 13B. Although the nanocomposite sample annealed below 175 °C does not exhibit a measurable Hall effect response (Figures 12B and 13B), considering the relatively constant carrier concentrations in the nanocomposite films, the onset of conductivity at ~200 °C processing is attributed to

11590

dx.doi.org/10.1021/ja301941q | J. Am. Chem. Soc. 2012, 134, 11583−11593

increases in carrier mobility. Furthermore, note that an onset in conductivity is observed for the combustion precursor films near 250 °C, and this can be attributed to free carrier generation over the percolation threshold ($>10^{20}$ cm$^{-3}$) due to dopant activation and oxygen vacancy generation.[40] For the combustion precursor-based films, all of the carriers must be provided by a single phase, while for the nanocomposite films, Fermi level alignment via carrier injection from the highly doped ITO nanoparticles into the undoped ITO combustion binder is expected. These injected carriers can then fill up the trap sites in the undoped ITO binder. As a result, lower reductive treatment temperatures are sufficient to afford high mobilities in the nanocomposite films. For the nanocomposite films subjected to H$_2$ treatment above 200 °C, all samples show significant carrier concentration increases, from $1-2 \times 10^{20}$ to $3 \times 10^{20}$ cm$^{-3}$. Considering the relatively small carrier concentration differences, $\sim$1.5–3.0 times, between the as-prepared and reduced nanocomposite films, the conductivity increase of typically >10-fold is attributed to the significant enhancement in mobility.

## CONCLUSIONS

Applying appropriate induction periods, acetylacetone-nitrate-based In$_2$O$_3$, ZnO, and ITO combustion precursors can be ignited at lower temperatures ($\sim$150 °C) than those typically required for continuously heated samples ($\sim$200 °C). The present study of the sample size and kinetic dependence of combustion precursor film formation indicates that sufficiently thick films and rapid heating profiles are essential for ignition of combustion in thin-film samples.

ZnO and ITO nanocomposite films with good transport properties were synthesized using oxide nanomaterials and the corresponding combustion precursors with ignition of the combustion precursors occurring at temperatures as low as 150 °C. The combustion precursor overlayer/impregnation coating process converts the porous and electrically disconnected nanomaterial films into dense, electrically connected films at remarkably low processing temperatures. To confirm that charge-transport enhancement is possible in properly processed nanomaterials, ZnO nanorod-based TFTs are fabricated. The as-deposited ZnO nanorod devices afford electron mobilities of $10^{-2}-10^{-3}$ cm$^2$ V$^{-1}$ s$^{-1}$. However, when the nanorod films are overcoated/impregnated with the ZnO combustion precursor, the electron mobility is increased to $\sim$0.2 cm$^2$ V$^{-1}$ s$^{-1}$. Moreover, oxygen vacancy generation and dopant activation are independently controlled at the oxide nanomaterial synthesis stage. Thus, commercially available ITO nanoparticles with high carrier concentrations are successively combined with the combustion precursor to produce transparent conducting films. The conductivity achieved at 150 °C is $\sim$10 S cm$^{-1}$ without a post-reductive treatment. In comparison, ITO combustion precursor- or ITO nanoparticle-based films require reductive H$_2$ treatment at 225 °C to achieve similar conductivity. Hall effect measurements on these ITO films verify the electron-transport enhancement and preservation of the predefined nanoparticle intrinsic properties during composite fabrication.

Importantly, a significant reduction in the processing temperature is demonstrated in this work for large-area metal oxide film fabrication along with a detailed understanding of the acetylacetone fuel-based combustion process and its application as a nanomaterial structural and electrical linker. We believe this novel composite approach can be extended to a variety of other functional nanomaterials with a diverse set of optical, magnetic, and/or electrical properties.

## ASSOCIATED CONTENT

**Ⓢ Supporting Information**

TGA-MS, AFM and SEM images, GIAXRD scans, and XPS spectra. This material is available free of charge via the Internet at http://pubs.acs.org.

## AUTHOR INFORMATION

**Corresponding Author**

m-kanatzidis@northwestern.edu (M.G.K.); a-facchetti@northwestern.edu (A.F.); t-marks@northwestern.edu (T.J.M.)

**Present Address**

§Korea Center for Artificial Photosynthesis, Center for Nano Materials, Sogang University, Seoul 121-742, Korea

**Notes**

The authors declare no competing financial interest.

## REFERENCES

(1) (a) Lany, S.; Zakutayev, A.; Mason, T. O.; Wager, J. F.; Poeppelmeier, K. R.; Perkins, J. D.; Berry, J. J.; Ginley, D. S.; Zunger, A. *Phys. Rev. Lett.* **2012**, 108. (b) Ko, S. W.; Verploegen, E.; Hong, S.; Mondal, R.; Hoke, E. T.; Toney, M. F.; McGehee, M. D.; Bao, Z. N. *J. Am. Chem. Soc.* **2011**, *133*, 16722. (c) Bettinger, C. J.; Becerril, H. A.; Kim, D. H.; Lee, B. L.; Lee, S.; Bao, Z. A. *Adv. Mater.* **2011**, *23*, 1257. (d) Goetz, K. P.; Li, Z.; Ward, J. W.; Bougher, C.; Rivnay, J.; Smith, J.; Conrad, B. R.; Parkin, S. R.; Anthopoulos, T. D.; Salleo, A.; Anthony, J. E.; Jurchescu, O. D. *Adv. Mater.* **2011**, *23*, 3698. (e) Marks, T. J. *MRS Bull.* **2010**, *35*, 1018. (f) Kim, S.; Ju, S.; Back, J. H.; Xuan, Y.; Ye, P. D.; Shim, M.; Janes, D. B.; Mohammadi, S. *Adv. Mater.* **2009**, *21*, 564. (g) Ginley, D. S.; Bright, C. *MRS Bull.* **2000**, *25*, 15.

(2) (a) Lee, M.; Williams, J. R.; Zhang, S. P.; Frisbie, C. D.; Goldhaber-Gordon, D. *Phys. Rev. Lett.* **2011**, 107. (b) Lee, C.; Srisungsitthisunti, P.; Park, S.; Kim, S.; Xu, X. F.; Roy, K.; Janes, D. B.; Zhou, C. W.; Ju, S.; Qi, M. H. *ACS Nano* **2011**, *5*, 1095. (c) Labram, J. G.; Kirkpatrick, J.; Bradley, D. D. C.; Anthopoulos, T. D. *Phys. Rev. B* **2011**, *84*, 075344. (d) Dacuña, J.; Salleo, A. *Phys. Rev. B* **2011**, *84*, 195209. (e) Sirringhaus, H.; Bird, M.; Richards, T.; Zhao, N. *Adv. Mater.* **2010**, *22*, 3893.

(3) (a) Rivnay, J.; Noriega, R.; Kline, R. J.; Salleo, A.; Toney, M. F. *Phys. Rev. B* **2011**, *84*, 045203. (b) Rivnay, J.; Steyrleuthner, R.; Jimison, L. H.; Casadei, A.; Chen, Z. H.; Toney, M. F.; Facchetti, A.; Neher, D.; Salleo, A. *Macromolecules* **2011**, *44*, 5246. (c) Ellison, D. J.; Lee, B.; Podzorov, V.; Frisbie, C. D. *Adv. Mater.* **2011**, *23*, 502. (d) Adamopoulos, G.; Bashir, A.; Gillin, W. P.; Georgakopoulos, S.; Shkunov, M.; Baklar, M. A.; Stingelin, N.; Bradley, D. D. C.; Anthopoulos, T. D. *Adv. Funct. Mater.* **2011**, *21*, 525. (e) Kang, M. S.; Sahu, A.; Norris, D. J.; Frisbie, C. D. *Nano Lett.* **2010**, *10*, 3727.

(4) (a) Walker, S. B.; Lewis, J. A. *J. Am. Chem. Soc.* **2012**, *134*, 1419. (b) Pasquarelli, R. M.; Ginley, D. S.; O'Hayre, R. *Chem. Soc. Rev.* **2011**, *40*, 5406. (c) Ahn, B. Y.; Lorang, D. J.; Duoss, E. B.; Lewis, J. A. *Chem. Commun.* **2010**, *46*, 7118. (d) Baklar, M. A.; Koch, F.; Kumar, A.; Domingo, E. B.; Campoy-Quiles, M.; Feldman, K.; Yu, L. Y.; Wobkenberg, P.; Ball, J.; Wilson, R. M.; McCulloch, I.; Kreouzis, T.;

Heeney, M.; Anthopoulos, T.; Smith, P.; Stingelin, N. *Adv. Mater.* **2010**, *22*, 3942. (e) Adamopoulos, G.; Bashir, A.; Thomas, S.; Gillin, W. P.; Georgakopoulos, S.; Shkunov, M.; Baklar, M. A.; Stingelin, N.; Maher, R. C.; Cohen, L. F.; Bradley, D. D. C.; Anthopoulos, T. D. *Adv. Mater.* **2010**, *22*, 4764. (f) Mitzi, D. B. *Solution Processing of Inorganic Materials*; Wiley: Hoboken, NJ, 2009. (g) Cho, J. H.; Lee, J.; Xia, Y.; Kim, B.; He, Y. Y.; Renn, M. J.; Lodge, T. P.; Frisbie, C. D. *Nat. Mater.* **2008**, *7*, 900. (h) Reuss, R. H.; Chalamala, B. R.; Moussessian, A.; Kane, M. G.; Kumar, A.; Zhang, D. C.; Rogers, J. A.; Hatalis, M.; Temple, D.; Moddel, G.; Eliasson, B. J.; Estes, M. J.; Kunze, J.; Handy, E. S.; Harmon, E. S.; Salzman, D. B.; Woodall, J. M.; Alam, M. A.; Murthy, J. Y.; Jacobsen, S. C.; Olivier, M.; Markus, D.; Campbell, P. M.; Snow, E. *Proc. IEEE* **2005**, *93*, 1239.

(5) (a) Jeong, S.; Moon, J. *J. Mater. Chem.* **2012**, *22*, 1243. (b) Fortunato, E.; Martins, R. *Phys. Status Solidi RRL* **2011**, *5*, 336. (c) Jiang, K.; Anderson, J. T.; Hoshino, K.; Li, D.; Wager, J. F.; Keszler, D. A. *Chem. Mater.* **2011**, *23*, 945. (d) Medvedeva, J. E. Combining Optical Transparency with Electrical Conductivity: Challenges and Prospects. In *Transparent Electronics: From Synthesis to Applications*; Facchetti, A., Marks, T. J., Eds.; Wiley: Chichester, West Sussex, U.K.; Hoboken, NJ, 2010; p 1. (e) Hosono, H. Transparent Oxide Semiconductors: Fundamentals and Recent Progress. In *Transparent Electronics: from Synthesis to Applications*; Facchetti, A., Marks, T. J., Eds.; Wiley: Chichester, West Sussex, U.K.; Hoboken, NJ, 2010; p 31. (f) Kamiya, T.; Hosono, H. *NPG Asia Mater.* **2010**, *2*, 15. (g) Pal, B. N.; Dhar, B. M.; See, K. C.; Katz, H. E. *Nat. Mater.* **2009**, *8*, 898. (h) Jeong, Y. T.; Dodabalapur, A. *Appl. Phys. Lett.* **2007**, 91. (i) Wager, J. F.; Keszler, D. A.; Presley, R. E. *Transparent Electronics*; Springer: New York, 2007. (j) Jones, A. C.; Aspinall, H. C.; Chalker, P. R.; Potter, R. J.; Manning, T. D.; Loo, Y. F.; O'Kane, R.; Gaskell, J. M.; Smith, L. M. *Chem. Vap. Deposition* **2006**, *12*, 83. (k) Robertson, J. *Eur. Phys. J. Appl. Phys.* **2004**, *28*, 265. (l) Wager, J. F. *Science* **2003**, *300*, 1245.

(6) (a) Ortiz, R. P.; Facchetti, A.; Marks, T. J. *Chem. Rev.* **2010**, *110*, 205. (b) Nomura, K.; Ohta, H.; Takagi, A.; Kamiya, T.; Hirano, M.; Hosono, H. *Nature* **2004**, *432*, 488. (c) Wang, A.; Babcock, J. R.; Edleman, N. L.; Metz, A. W.; Lane, M. A.; Asahi, R.; Dravid, V. P.; Kannewurf, C. R.; Freeman, A. J.; Marks, T. J. *Proc. Natl. Acad. Sci. U.S.A.* **2001**, *98*, 7113.

(7) (a) Song, K.; Noh, J.; Jun, T.; Jung, Y.; Kang, H. Y.; Moon, J. *Adv. Mater.* **2010**, *22*, 4308. (b) Lee, C. G.; Dodabalapur, A. *Appl. Phys. Lett.* **2010**, *96*, 243501. (c) Subramanian, V. Solution-Processed Electronics Based on Transparent Conductive Oxides. In *Transparent Electronics: From Synthesis to Applications*, Facchetti, A., Marks, T. J., Eds.; Wiley: Chichester, West Sussex, U.K.; Hoboken, NJ, 2010. (d) Kim, M. G.; Kim, H. S.; Ha, Y. G.; He, J. Q.; Kanatzidis, M. G.; Facchetti, A.; Marks, T. J. *J. Am. Chem. Soc.* **2010**, *132*, 10352. (e) Kim, H. S.; Kim, M. G.; Ha, Y. Q.; Kanatzidis, M. G.; Marks, T. J.; Facchetti, A. *J. Am. Chem. Soc.* **2009**, *131*, 10826. (f) Kim, H. S.; Byrne, P. D.; Facchetti, A.; Marks, T. J. *J. Am. Chem. Soc.* **2008**, *130*, 12580. (g) Meyers, S. T.; Anderson, J. T.; Hung, C. M.; Thompson, J.; Wager, J. F.; Keszler, D. A. *J. Am. Chem. Soc.* **2008**, *130*, 17603. (h) Sun, B. Q.; Peterson, R. L.; Sirringhaus, H.; Mori, K. *J. Phys. Chem. C* **2007**, *111*, 18831. (i) Aoki, Y.; Kunitake, T.; Nakao, A. *Chem. Mater.* **2005**, *17*, 450. (j) Niesen, T. P.; De Guire, M. R. *Solid State Ionics* **2002**, *151*, 61.

(8) (a) Talapin, D. V.; Lee, J. S.; Kovalenko, M. V.; Shevchenko, E. V. *Chem. Rev.* **2010**, *110*, 389. (b) Clifford, J. P.; Konstantatos, G.; Johnston, K. W.; Hoogland, S.; Levina, L.; Sargent, E. H. *Nat. Nanotechnol.* **2009**, *4*, 40. (c) Caruge, J. M.; Halpert, J. E.; Wood, V.; Bulovic, V.; Bawendi, M. G. *Nature Photon.* **2008**, *2*, 247. (d) Talapin, D. V.; Murray, C. B. *Science* **2005**, *310*, 86. (e) Gur, I.; Fromer, N. A.; Geier, M. L.; Alivisatos, A. P. *Science* **2005**, *310*, 462.

(9) (a) Borchert, H. *Energy Environ. Sci.* **2010**, *3*, 1682. (b) Kovalenko, M. V.; Scheele, M.; Talapin, D. V. *Science* **2009**, *324*, 1417. (c) Ridley, B. A.; Nivi, B.; Jacobson, J. M. *Science* **1999**, *286*, 746.

(10) (a) Li, S. S.; Chang, C. P.; Lin, C. C.; Lin, Y. Y.; Chang, C. H.; Yang, J. R.; Chu, M. W.; Chen, C. W. *J. Am. Chem. Soc.* **2011**, *133*, 11614. (b) Richter, T. V.; Stelzl, F.; Schulz-Gericke, J.; Kerscher, B.; Wurfel, U.; Niggemann, M.; Ludwigs, S. *J. Mater. Chem.* **2010**, *20*, 874.

(c) Walther, S.; Schafer, S.; Jank, M. P. M.; Thiem, H.; Peukert, W.; Frey, L.; Ryssel, H. *Microelectron. Eng.* **2010**, *87*, 2312. (d) Gross, M.; Winnacker, A.; Wellmann, P. J. *Thin Solid Films* **2007**, *515*, 8567. (e) Lee, S.; Jeong, S.; Kim, D.; Park, B. K.; Moon, J. *Superlattices Microstruct.* **2007**, *42*, 361. (f) Huynh, W. U.; Dittmer, J. J.; Libby, W. C.; Whiting, G. L.; Alivisatos, A. P. *Adv. Funct. Mater.* **2003**, *13*, 73.

(11) (a) Al-Dahoudi, N.; Aegerter, M. A. *Thin Solid Films* **2006**, *502*, 193. (b) Goebbert, C.; Nonninger, R.; Aegerter, M. A.; Schmidt, H. *Thin Solid Films* **1999**, *351*, 79.

(12) Sun, B. Q.; Sirringhaus, H. *J. Am. Chem. Soc.* **2006**, *128*, 16231.

(13) Zabet-Khosousi, A.; Dhirani, A. A. *Chem. Rev.* **2008**, *108*, 4072.

(14) Leibowitz, F. L.; Zheng, W. X.; Maye, M. M.; Zhong, C. J. *Anal. Chem.* **1999**, *71*, 5076.

(15) Lee, J. S.; Kovalenko, M. V.; Huang, J.; Chung, D. S.; Talapin, D. V. *Nat. Nanotechnol.* **2011**, *6*, 348.

(16) (a) Mitzi, D. B.; Copel, M.; Murray, C. E. *Adv. Mater.* **2006**, *18*, 2448. (b) Mitzi, D. B.; Copel, M.; Chey, S. J. *Adv. Mater.* **2005**, *17*, 1285.

(17) (a) Kim, M.-G.; Kanatzidis, M. G.; Facchetti, A.; Marks, T. J. *Nat. Mater.* **2011**, *10*, 382. (b) Hennek, J. W.; Kim, M.-G.; Kanatzidis, M. G.; Facchetti, A.; Marks, T. J. *J. Am. Chem. Soc.* **2012**, *134*, 9593.

(18) Jun, J. H.; Park, B.; Cho, K.; Kim, S. *Nanotechnology* **2009**, *20*, 505201.

(19) (a) Hoefer, U.; Frank, J.; Fleischer, M. *Sens. Actuators B* **2001**, *78*, 6. (b) Barsan, N.; Weimar, U. *J. Electroceram.* **2001**, *7*, 143.

(20) Okamura, K.; Nikolova, D.; Mechau, N.; Hahn, H. *Appl. Phys. Lett.* **2009**, *94*, 183503.

(21) Greve, D. W. *Field Effect Devices and Application: Devices for Portable, Low-Power, and Imaging Systems*; Prentice-Hall: NJ, 1988.

(22) Erri, P.; Pranda, P.; Varma, A. *Ind. Eng. Chem. Res.* **2004**, *43*, 3092.

(23) (a) Hosono, H. *J. Non-Cryst. Solids* **2006**, *352*, 851. (b) Minami, T. *MRS Bull.* **2000**, *25*, 38.

(24) (a) Epifani, M.; Melissano, E.; Pace, G.; Schioppa, M. *J. Eur. Ceram. Soc.* **2007**, *27*, 115. (b) Vonhoene, J.; Charles, R. G.; Hickam, W. M. *J. Phys. Chem.* **1958**, *62*, 1098.

(25) Zaslonko, I. S.; Kogarko, S. M.; Mozzhukhin, E. V. *Combust. Explo. Shock Waves* **1973**, *9*, 295.

(26) Sato, T. *J. Therm. Anal. Calorim.* **2005**, *82*, 775.

(27) (a) Adurodija, F. O.; Semple, L.; Bruning, R. *J. Mater. Sci.* **2006**, *41*, 7096. (b) Morikawa, H.; Fujita, M. *Thin Solid Films* **2000**, *359*, 61.

(28) (a) Jeong, S.; Ha, Y.-G.; Moon, J.; Facchetti, A.; Marks, T. J. *Adv. Mater.* **2010**, *22*, 1346. (b) Donley, C.; Dunphy, D.; Paine, D.; Carter, C.; Nebesny, K.; Lee, P.; Alloway, D.; Armstrong, N. R. *Langmuir* **2002**, *18*, 450.

(29) (a) Houston, P. L., *Chemical Kinetics and Reaction Dynamics*; Dover Publications: Mineola, NY, 2006. (b) Schott, G. L.; Kinsey, J. L. *J. Chem. Phys.* **1958**, *29*, 1177.

(30) Voropanova, L. A.; Baratov, L. G.; Kovalev, V. N. *Russ. J. Appl. Chem.* **2010**, *83*, 1925.

(31) Ong, B. S.; Li, C. S.; Li, Y. N.; Wu, Y. L.; Loutfy, R. *J. Am. Chem. Soc.* **2007**, *129*, 2750.

(32) Sun, B.; Sirringhaus, H. *Nano Lett.* **2005**, *5*, 2408.

(33) (a) Patil, K. C.; Aruna, S. T.; Ekambaram, S. *Curr. Opin. Solid State Mater. Sci.* **1997**, *2*, 158. (b) Patil, K. C.; Aruna, S. T.; Mimani, T. *Curr. Opin. Solid State Mater. Sci.* **2002**, *6*, 507. (c) Yi, H. C.; Moore, J. J. *J. Mater. Sci.* **1990**, *25*, 1159.

(34) (a) Gilstrap, R. A.; Capozzi, C. J.; Carson, C. G.; Gerhardt, R. A.; Summers, C. J. *Adv. Mater.* **2008**, *20*, 4163. (b) Seo, W. S.; Jo, H. H.; Lee, K.; Park, J. T. *Adv. Mater.* **2003**, *15*, 795. (c) Shim, M.; Guyot-Sionnest, P. *J. Am. Chem. Soc.* **2001**, *123*, 11651. (d) Meulenkamp, E. A. *J. Phys. Chem. B* **1998**, *102*, 5566.

(35) Ederth, J.; Johnsson, P.; Niklasson, G. A.; Hoel, A.; Hultaker, A.; Heszler, P.; Granqvist, C. G.; van Doorn, A. R.; Jongerius, M. J.; Burgard, D. *Phys. Rev. B* **2003**, *68*, 155410.

(36) Murphy, C. J. *J. Cluster Sci.* **1996**, *7*, 341.

(37) (a) Sasaki, T.; Endo, Y.; Nakaya, M.; Kanie, K.; Nagatomi, A.; Tanoue, K.; Nakamura, R.; Muramatsu, A. *J. Mater. Chem.* **2010**, *20*, 8153. (b) Hoertz, P. G.; Chen, Z. F.; Kent, C. A.; Meyer, T. J. *Inorg.*

*Chem.* **2010**, *49*, 8179. (c) Kanehara, M.; Koike, H.; Yoshinaga, T.; Teranishi, T. *J. Am. Chem. Soc.* **2009**, *131*, 17736. (d) Ba, J. H.; Fattakhova-Rohlfing, D.; Feldhoff, A.; Brezesinski, T.; Djerdj, I.; Wark, M.; Niederberger, M. *Chem. Mater.* **2006**, *18*, 2848.

(38) (a) Puetz, J.; Al-Dahoudi, N.; Aegerter, M. A. *Adv. Eng. Mater.* **2004**, *6*, 733. (b) Alam, M. J.; Cameron, D. C. *Thin Solid Films* **2002**, *420*, 76.

(39) (a) Yaglioglu, B.; Huang, Y. J.; Yeom, H. Y.; Paine, D. C. *Thin Solid Films* **2006**, *496*, 89. (b) Lee, C.; Lee, W.; Kim, H.; Kim, H. W. *Ceram. Int.* **2008**, *34*, 1089. (c) Morgan, D. V.; Aliyu, Y. H.; Bunce, R. W.; Salehi, A. *Thin Solid Films* **1998**, *312*, 268.

(40) (a) Reddy, V. S.; Das, K.; Dhar, A.; Ray, S. K. *Semicond. Sci. Technol.* **2006**, *21*, 1747. (b) Hu, Y. L.; Diao, X. G.; Wang, C.; Hao, W. C.; Wang, T. M. *Vacuum* **2004**, *75*, 183. (c) Adurodija, F. O.; Izumi, H.; Ishihara, T.; Yoshioka, H.; Motoyama, M.; Murai, K. *J. Vac. Sci. Technol. A* **2000**, *18*, 814.